Engineered Science
DOI: https://dx.doi.org/10.30919/es1435

Solar Thermal Performance: Using Perforated, Corrugated, Waved and Punched Absorber Plates

Noor Samir Lafta, Afaq Jasim Mahmood,* Kadhum Audaa Jehhef and Fadhil Abdulrazzaq Kareem

Abstract

The heat transfer and thermal efficiency of a solar air heater are diminished due to the low thermal conductivity of air. Using various artificial roughness geometries has proven effective in increasing the heat contact surface area. In this study, two double-pass glazed solar heaters, equipped with perforated and corrugated absorber plates, are then changed to wavy and punched absorber plates. Experimental and numerical modeling are conducted to assess the effects of inlet temperature, solar intensity, and airflow rate on the outlet temperature and thermal efficiency. Thermal efficiencies significantly increase at higher flow rates, but heat loss from the absorber plate to the surroundings also becomes more pronounced at an airflow rate of 0.035 kg/s, for perforated, wavy, corrugated, and punched collectors are 0.76, 0.62, 0.52, and 0.394% respectively. However, the highest outlet temperatures are recorded at a minimum airflow rate of 0.017 kg/s, with perforated and corrugate heaters reaching 66.7 and 60.6 °C, wave and punched heaters reaching 59.9 and 51.8 °C. Additionally, the findings reveal a notable enhancement in outlet temperature when using a perforated absorber plate, compared to corrugated, wavy, and punched absorber plates. Additionally, empirical formulas for thermal efficiencies and outlet temperatures are developed based on the theoretical model.

Keywords: Solar air heater; Double pass; Thermal efficiency; Perforated and corrugated absorber plate; Wavy and punched collectors.
Received: 06 December 2024; Revised: 27 January 2025; Accepted: 16 February 2025.
Article type: Research article.

1. Introduction

Iraq possesses abundant solar energy, a clean and dependable power source that is freely available and offers numerous applications. By harnessing solar energy, individuals can reduce their energy bills and decrease reliance on fossil fuels, thereby minimizing pollution risks. In recent years, solar energy has emerged as a viable alternative to traditional, environmentally harmful fuels. The simplest method of utilizing solar energy involves converting the sun's heat into thermal energy, which is achieved through the use of solar cells. These panels capture sunlight and transform it into usable thermal energy.[1] Flat panel solar collectors are a durable and effective technology for capturing solar energy.

These systems typically include several key components: a transparent glass cover, absorber panels with a selective coating, insulation layers, sealants, and a structural frame. The efficiency of converting solar radiation into usable thermal energy with flat plate collectors is primarily influenced by the careful design and integration of these elements.[2] Several physical factors, such as air flow rate, flow direction, solar intensity, collector size, cover plate properties, and wind speed, influence the performance of solar collectors. However, the key parameters that are crucial for a solar collector's efficiency are the absorber area, airflow characteristics, and cover plate.[3] Many researchers have explored ways to enhance solar heating systems. One notable approach is the use of a corrugated absorber plate, which has demonstrated significant improvements in heat storage and release, particularly in the absence of solar radiation. Studies conducted under the climatic conditions of Iraq (36.348 °N, 43.1577 °E) revealed that a modified solar collector with a corrugated design achieved higher thermal efficiency than the standard collector. This design improved heat retention, reduced energy losses, and increased the temperature difference between the inlet and outlet air, thereby significantly enhancing the thermal performance and energy storage capacity of solar air heaters (SAHs), as emphasized in earlier studies.[4] A recent study, in 2024, A.Sreeharsha *et al.*[5] investigated the thermal performance of solar air collectors equipped with smooth and V-shaped corrugated absorber panels. Using three-dimensional computational fluid dynamics (3D CFD) analysis, various Reynolds numbers and corrugation patterns were examined. The V-shaped corrugated design outperformed the

Middle Technical University, Baghdad, 10001, Iraq
**Email:* Dr.Afaq_jasem100@mtu.edu.iq (A. J. Mahmood)

smooth configuration, achieving a maximum outlet temperature of 61 °C and a thermal efficiency of 46.7%, compared to 53 °C and 33.01% for the smooth design. These findings highlight the significant enhancement in heat transfer and efficiency offered by the V-shaped corrugated configuration, making it a highly effective option for solar air heating systems.

Other researchers have advanced solar heating applications by developing dual-flow SAHs featuring various absorber designs.[6] Numerical analyses revealed that dual-flow systems with corrugated absorbers outperformed flat plate designs in terms of energy efficiency. The highest improvement in energy efficiency was observed at a high air flow rate at a mass flow rate of 0.0046 kg/s.[7] However, at mass flow rates exceeding 0.072 kg/s, energy efficiency declined and eventually became negative.[8] The study, in 2024, by Gitan and Mohammed also highlighted that increased solar intensity enhanced air temperature rise and overall efficiency across all configurations, with more significant improvements occurring at lower mass flow rates.[9] An experimental study was carried out to evaluate the performance of a double-pass perforated solar collector, considering the interaction between Reynolds number and perforation ratio for different perforation levels. At a low Reynolds number of approximately 10,000, reducing the perforation ratio from 7 to 3 resulted in an increase in thermal efficiency by about 4%.[10] Notably, this effect became more pronounced as the Reynolds number increased to higher levels.[11] According to the study, dual-flow SAHs with the perforated absorber demonstrated higher efficiency compared to conventional designs and delivered the best performance.[12] Among the tested configurations, the perforated absorber exhibited the highest thermal efficiency, making it the most effective design. In 2020, the results of Mahmood revealed that a maximum efficiency of 62.50% was achieved using a 7.5 cm high collector in the double-pass SAH, compared to 55% efficiency in the single-pass SAH.[13] Additionally, a double-pass SAH was further enhanced by incorporating artificial roughness with various configurations to improve its thermal performance.[14] In 2022, Alomar *et al*.[15] investigated various configurations of corrugated perforated absorber plates and fluid flow channels to determine the optimal combination for maximizing the thermal efficiency of SAHs. The study involved experiments on a double-pass SAH, where fluid flow occurred both above and below the absorber plate. The highest thermal efficiency, 66.7%, was achieved with a corrugated perforated absorber plate, with the majority of the flow directed above the plate. The findings revealed that flow with punched burrs absorber plate enhanced fluid mixing, heat transfer, and overall efficiency compared to continuous burrs,[16] the punched burrs demonstrated a significantly higher thermal performance coefficient compared to the continuous design, highlighting the effectiveness of perforated wavy configurations in enhancing the efficiency of SAHs. This research emphasizes the need for further studies to refine and optimize thermal performance.[17,18] Additionally, in 2015, Priyam and Chand investigated two transversely positioned wavy fins attached to the absorber plate, and their work led to the development of expressions for the collector efficiency factor of such systems.[19]

Previous studies suggest that the thermal performance of solar systems can be significantly enhanced by using either perforated or corrugated plates, both known for their high efficiency. While many investigations have individually analyzed the effects of these plate designs, no study has yet combined them in a single analysis. This research is the first to evaluate the thermal performance of combined corrugated and perforated assemblies under identical outdoor conditions, testing four configurations to determine the most effective design for optimizing thermal efficiency.

2. Experimental setup

Four double pass flat-plate SAHs were designed and constructed at the Middle Technical University, Institute of Technology Baghdad, located at 33.33 °N, 44.43 °E in Baghdad, Iraq. The investigation involved designing four wooden collectors facing south at 38° to maximize sun exposure for over seven hours per day. Key components of the SAHs include the absorber plate area and the cover, both aimed at enhancing the heat transfer rate and airflow characteristics. The solar heaters were built using punched, wavy, perforated, and corrugated absorber plates, made of galvanized steel solid plates with a thickness of 1.5 mm, and a glass panel of 6 mm thickness (an area of 114×105 cm²) as covers. The glazed covers reduced heat loss to the surroundings, thereby improving the solar heater's thermal efficiency and the temperature of the exiting air. All sides of the solar duct and absorber plates were coated black to enhance the absorption of solar radiation. Fig. 1 presents both a photo and a schematic diagram of the experimental test rig. The rectangular wooden duct had an area of 114×109 cm², with a test section depth of 4.5 cm. Air enters the solar collectors through an inlet opening of 4 cm by 114 cm, then exits through a circular outlet with a diameter of 8.5 cm. The solar collector consists of the following key components:

1. Perforated, Corrugated, Wavy, and Punched Absorber Plates: These plates were installed horizontally, dividing the air flow into two separate passes, one with a 3.5 cm space above the absorber plates and another with a 2.2 cm space below. The design enhanced heat transfer by increasing turbulence and fluid mixing, which in turn improved thermal efficiency.
2. Double-Pass Solar Collector: This design typically aims to boost thermal efficiency by providing extended contact time with both the upper and lower absorber plates.
3. Glazed Cover: This component helps reduce heat loss from the top of the solar collectors.

A hot wire anemometer was used to measure airflow velocity at a stationary point within the delivery airflow section. Temperature data was recorded with an EXTECH instrument. A four-channel thermometer was equipped with four T-type thermocouples that were calibrated and positioned

Table 1: Specification of the collectors and equipment.

Description	Equipment
Baghdad-Iraq (33.33 °N and 44.43 °E)	Two bed, solar collectors, 114 cm × 109 cm × 4.5 cm, south, 40°
Solar intensity	Pyranometer RK200-03, Series: 0-2000 W/m^2.
Centrifugal fan	0.75 kW, Model 135C16A.
Outlet air delivered suction	Galvanized circular duct, 8 cm diameter.
Air flow rate	Hot wire anemometer, HT-9829, 60-90 mA.
Regulates the fan speed Inlet Air Suck suction area	Inverter (model SV008iC5-1, 0.01-400Hz, 5A)
Glazed cover	(4.5 × 114) cm^2 Area: (116 × 112) cm^2
Temperature measurement	(EXTECH) model SDL200. Data-logger. Accuracy of ± (0.4 % + 1 °C)

as follows: one for ambient temperature (located under the bed), one for inlet temperature (centered in the inlet groove area), and two for outlet temperature (placed at the center of the outlet airflow). A pyrometer measured solar intensity in watts per square meter, with data collection occurring from 8:00 am to 5:00 pm. The Pyranometer was mounted on the solar platform. The solar system operated as an active system, featuring a fan positioned at the back of the collector, and an inverter (model SV008iC5-1, 0.01-400 Hz, 5A) regulated the fan speed and airflow rate, which ranged from 0.021 to 0.037 m/s. Design and operating parameters are detailed in Table 1.

3. Thermal performance of solar collector

Useful heat gains for passing air through the solar channel can be expressed in terms of mean plate temperature using the following equations of Eqs. 1 and 2.[13,14]

$$Q_u = A_p[I(\tau\alpha) - U_L(Tp - Ta)] \quad (1)$$

Hottel-Whillier-Bliss equation can also be used to evaluate the heat gain of flowing air through the solar duct.[20-22]

$$Q_u = A_p F_R[I(\tau\alpha) - U_L(T_i - T_a)] \quad (2)$$

Heat removal factor F_R and thermal efficiency η_{th} as in Eqs. 3 and 4:

$$F_R = \frac{\dot{m}\, C_p}{U_L\, A_p}\left[1 - exp\left(\frac{U_L A_p\, F'}{\dot{m}\, C_p}\right)\right] \quad (3)$$

$$\eta_{th} = \frac{Q_u}{I.A_p} = F_R\left[(\tau\alpha) - U_L\left(\frac{T_i - T_a}{I}\right)\right] \quad (4)$$

Also, it can be written Eq. 5 in terms of air outlet temperature:

$$\eta_{th} = F_o\left[(\tau\alpha) - U_L\left(\frac{T_o - T_i}{I}\right)\right] \quad (5)$$

where the factor F_o can be evaluated as in Eq. 6:

$$F_o = \frac{\dot{m}\, C_p}{U_L\, A_p}\left[exp\left(\frac{U_L A_p\, F'}{\dot{m}\, C_p}\right) - 1\right] \quad (6)$$

Useful energy gain is evaluated as:

$$Q_u = \dot{m} C_p (T_o - T_i) \quad (7)$$

According to Eq. 7 the thermal efficiency is calculated as Eq. 8:

$$\eta_{th} = \frac{\dot{m}\, C_p (T_o - T_i)}{I\, A_p} \quad (8)$$

4. Experimental analysis

The research examined four types of SAHs, with outdoor experiments conducted over four consecutive days. Hourly measurements of inlet and outlet temperatures and solar radiation intensity were taken over ten hours from 8:00 a.m. to 4:00 p.m. The study assessed the thermal efficiency of collectors with wavy, corrugated, perforated, and punched galvanized absorber plates to determine the most efficient design. The experiments were conducted from March 3rd to March 8th, 2024, under clear skies with low wind conditions and varied airflow rates between 0.016 and 0.032 kg/s, consistent with existing studies on similar solar heaters

4.1 Solar intensity, inlet temperature, and outlet temperature

The hourly measurements of solar intensity and inlet air temperature were recorded over four experimental days, each conducted at different air flow rates. Figs. 2 and 3 illustrate the solar intensity curves over time at different airflow rates, respectively, which exhibited a consistent pattern across all working days. Solar intensity increased from sunrise to midday, reaching its peak at noon, and then gradually decreased until sunset. The solar intensity curves for all experimental days closely resembled each other, with maximum values ranging between 1007 and 1011 W/m^2. The highest inlet temperature and solar radiation values were observed between 12:00 and 1:00 pm, ranging from 30 to 32.5 °C.

Also, Figs. 2 and 3 show the inlet temperature (T_i), ambient temperature (T_a), and outlet temperature (T_o) throughout the day, spanning from 8:00 am to 4:00 pm, for five different absorber plates with airflow rates varying between 0.016 kg/s and 0.032 kg/s. The temperature trends for (T_i), (T_a), and (T_o) closely matched the pattern of solar intensity, reaching their peak at noon and gradually decreasing toward the evening. The inlet air temperature (T_i) was always higher than the ambient temperature (T_a). The ambient temperature was recorded in a shaded location beneath the bed, while (T_i) was

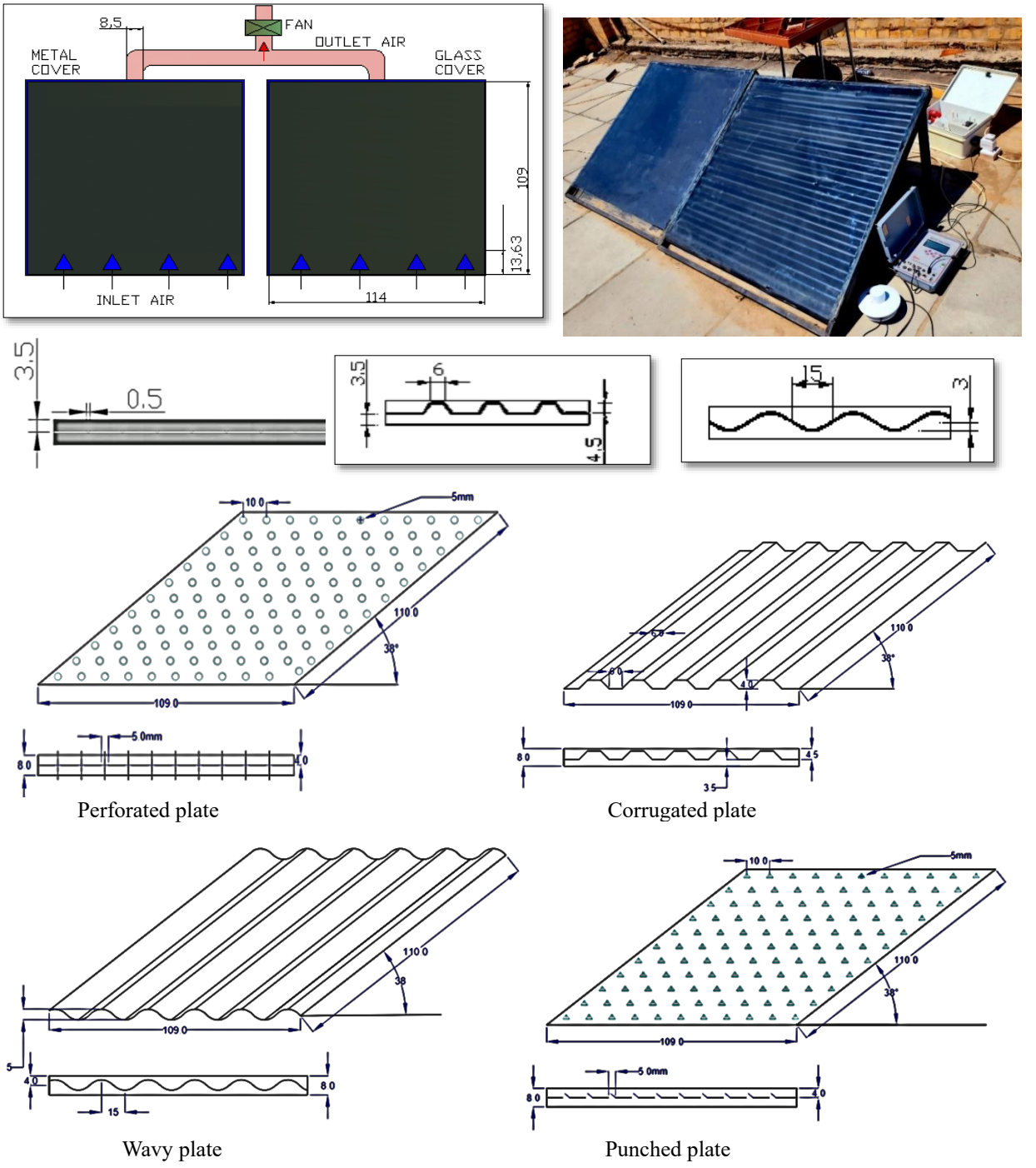

Fig. 1: Scheme and photos of the experimental work.

measured at the bed's inlet. This pattern was linked to the parallel-pass configuration of the glazed collector or the parallel air pass setup, where air is preheated in the upper channel before transferring heat to the lower channel. Additionally, the outlet temperature (T_o) increased as the airflow rate decreased from 0.032 to 0.016 kg/s. This was mainly due to the prolonged duration of air movement within the collector, allowing more time for heat absorption as the air traveled from the inlet to the outlet. In essence, the slower air velocity enabled greater heat transfer from the absorber plates to the flowing air. Table 2 provides the average values of ambient temperatures, inlet temperatures, outlet temperatures, and solar intensity across various airflow rates. Similar to the present study, Prashant *et al.*[21] analyzed the temperature curves for parallel flow systems, demonstrating that the outlet temperature increases with a decrease in airflow rate due to a longer residence time. The observed behavior in this study mirrors these findings, with outlet temperature strongly correlated with solar intensity.

4.2 Temperature differences for perforated, corrugated, wavy, and punched absorber plates over seven hours

Fig. 4 illustrates the variation in temperature difference ($\Delta T = T_o - T_a$) over time for different airflow rates ranging from

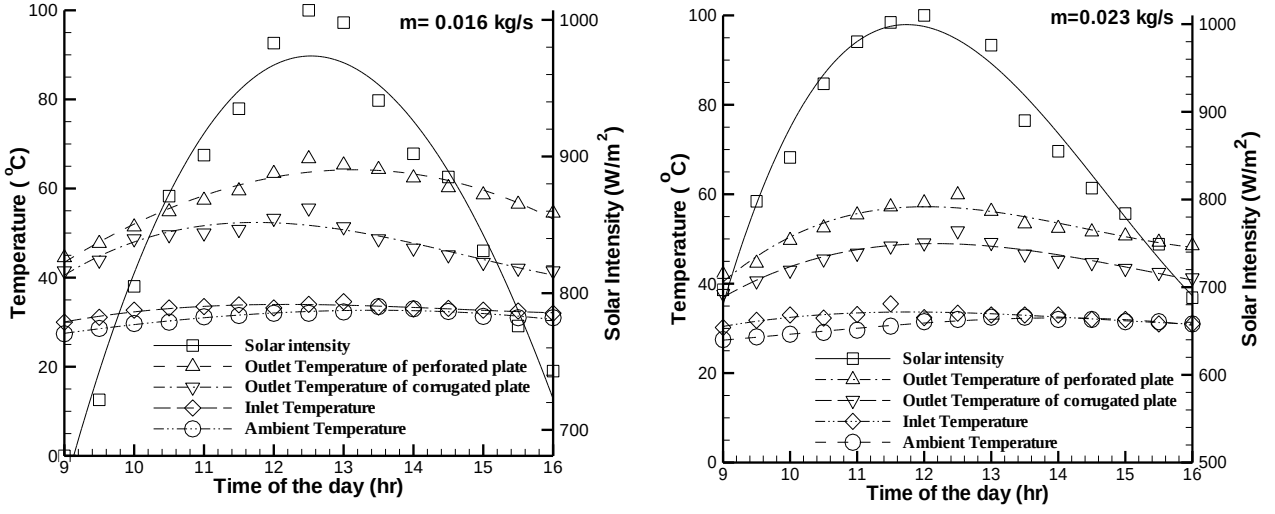

Fig. 2: Experimental measurements for solar intensity, inlet temperature, ambient temperature, and outlet temperature of perforated plate and corrugate plate.

Table 2: The average data of the ambient temperatures (T_a), inlet temperatures (T_i), outlet temperatures (T_o), and solar intensity (I), with different absorber plate shapes and air flow rates.

Absorber plate shape	$\dot{m}$ kg/s	I avr. W/m²	T_a avr. °C	T_i avr. °C	T_o avr. °C
Perforator1	0.016	865.4	31.1	32.8	58
Corrugate2					51
Perforator1	0.032	867.7	30.2	30.2	52
Corrugate2					46
Wavy1	0.016	876.5	30.6	32.4	51
Punched2					45
Wavy1	0.032	892.9	28.8	30.76	48
Punched2					41

0.016 to 0.023 kg/s. The temperature differences ($\Delta T = T_o - T_a$) for the four types of absorber plates-perforated, corrugated, wavy, and punched-were measured over a seven-hour period from 8:00 am to 4:00 pm.

- Perforated Plate: Achieved the highest temperature difference, peaking at 33.3 °C during noon under solar intensity of 1007 W/m², at an airflow rate of 0.016 kg/s.
- Corrugated Plate: Demonstrated slightly lower ΔT compared to the perforated plate, with a peak temperature difference close to 30 °C under similar conditions.
- Wavy Plate: Delivered a balanced performance, with a peak ΔT of approximately 31.5 °C, indicating efficient thermal absorption and heat retention.
- Punched Plate: Recorded the lowest temperature difference, peaking at 27 °C, showing reduced heat gain compared to other configurations.

The trend of ΔT across all absorber plates followed a consistent pattern: increasing steadily in the morning, reaching maximum values at noon, and gradually decreasing in the afternoon as solar intensity declined.

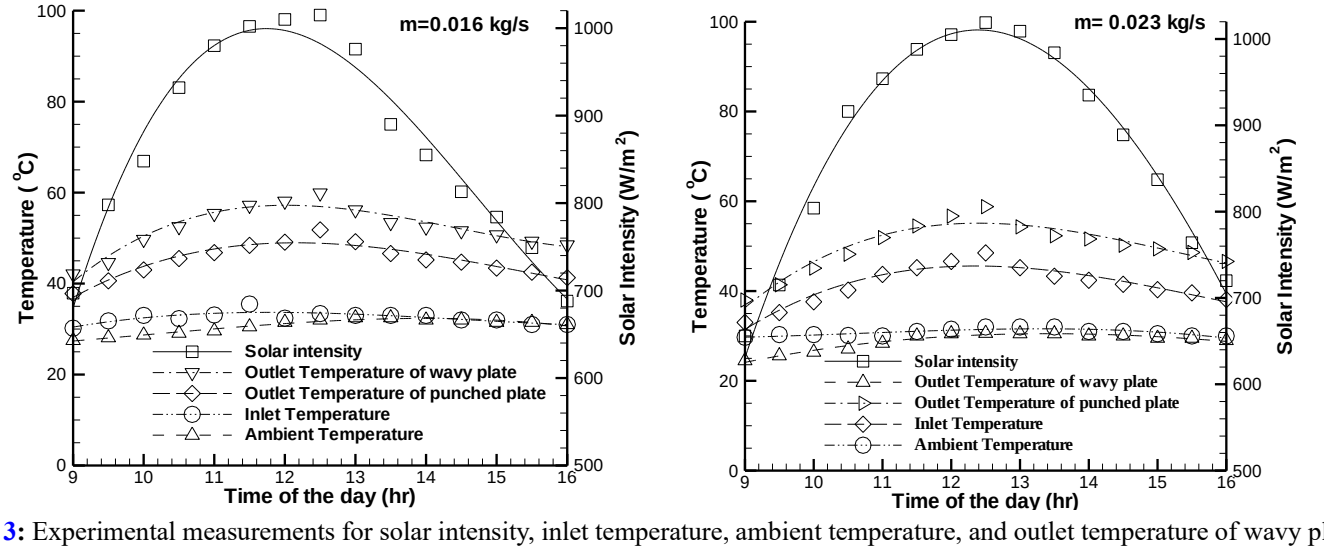

Fig. 3: Experimental measurements for solar intensity, inlet temperature, ambient temperature, and outlet temperature of wavy plate and punched plate.

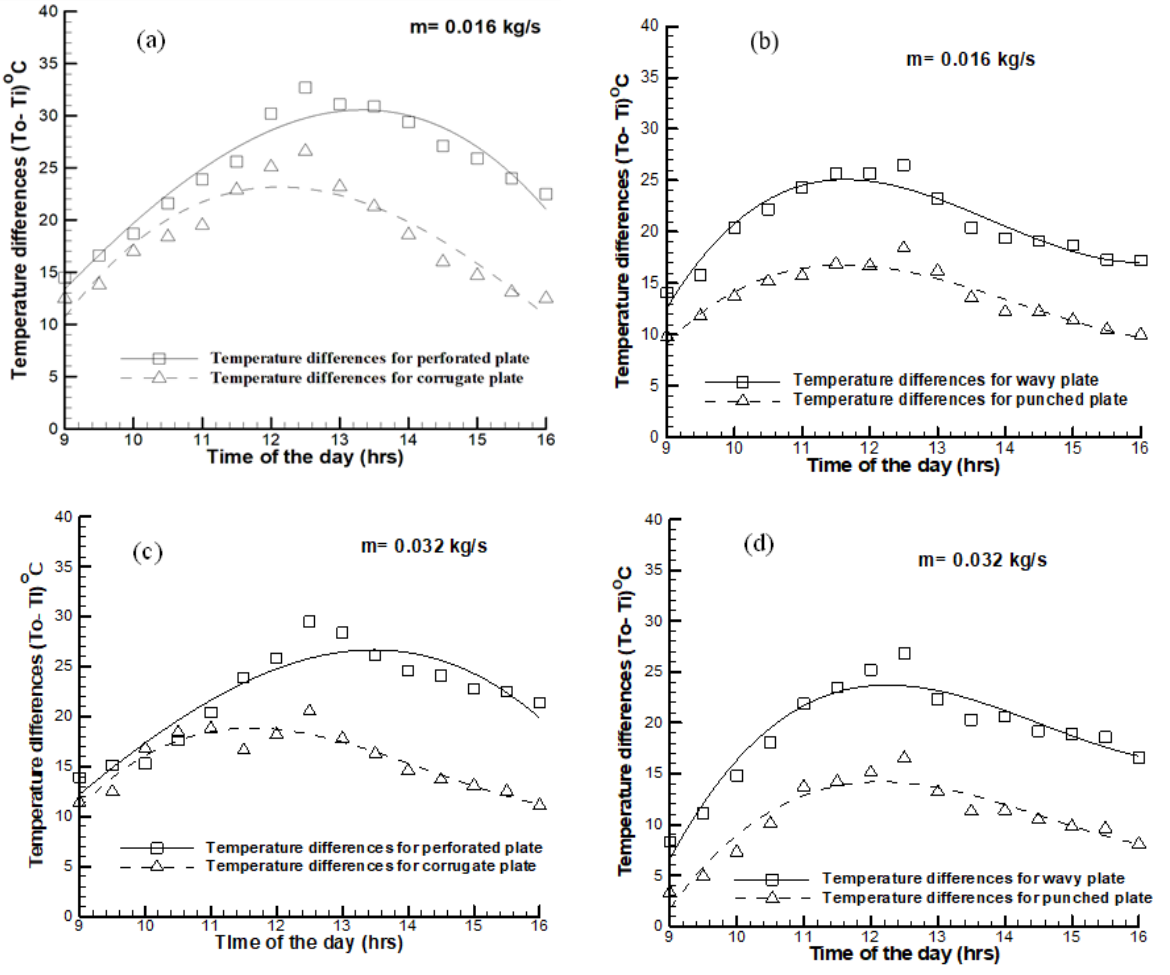

Fig. 4: Temperature differences for (a) perforated, corrugated for air flow rate m= 0.016 kg/s, (b) wavy, and punched absorber plates, for air flow rate m= 0.016 kg/s, (c) perforated, corrugated for air flow rate m= 0.032 kg/s, (d) wavy, and punched absorber plates, for air flow rate of 0.032 kg/s, over seven hours a day.

When temperature differences for perforated and corrugate plates were compared with the punched and wavy collectors, there was an enhancement in the heat transfer performance for perforated and corrugate plates compared to wavy and punched plates.

4.3 Instantaneous efficiencies corresponding to a temperature parameter (Ti–Ta)/I

From Eq. 4, a linear plot of efficiency versus the temperature parameter (Ti−Ta)/I was generated, where the slope represents (U_L), and the y-intercept represents (τα). It is important to note that U_L is not constant but depends on both the ambient temperature and the collector's outlet temperature. Figs. 5-8 illustrate the instantaneous thermal efficiency (ηi) of the collector plotted against (T_i−T_a)/I for airflow rates of 0.016 and 0.032 kg/s. The maximum efficiency recorded was 74% for the perforated solar collector, with a negative linear slope B = −5.46 and a correlation coefficient R^2 = 0.181 at 0.032 kg/s. In comparison, the maximum efficiency for the wavy collector was 64%, with a negative linear slope B = −3.669 and a correlation coefficient R^2 = 0.91 at the same airflow rate. Similar to the present study, Nowzari *et al.*[22] emphasized the role of perforated covers in enhancing thermal efficiency by reducing heat loss and improving airflow distribution, which aligns with the improved results observed for the perforated plate in this study.

4.4 The empirical expression derived for instantaneous efficiencies

The derived empirical formula for instantaneous efficiencies is presented as in Eq. 9:[13,14]

$$\eta_i = A + B\frac{(T_i - T_a)}{I} \quad (9)$$

where the factors A and B were determined from the analysis of the graphs shown in Figs. 5-8. Table 3 presents the empirical equations for thermal efficiencies corresponding to all cases examined in this study.

4.5 The empirical equations for outlet temperatures of different absorber plates

The computation of Eqs. 5 and 6 produces expressions for the outlet air temperature (T_o) as a function of the inlet air temperature (T_i) and the ambient temperature.[23]

$$T_o = (1 - B\lambda)T_i + B\lambda T_a + AI\lambda \quad (10)$$

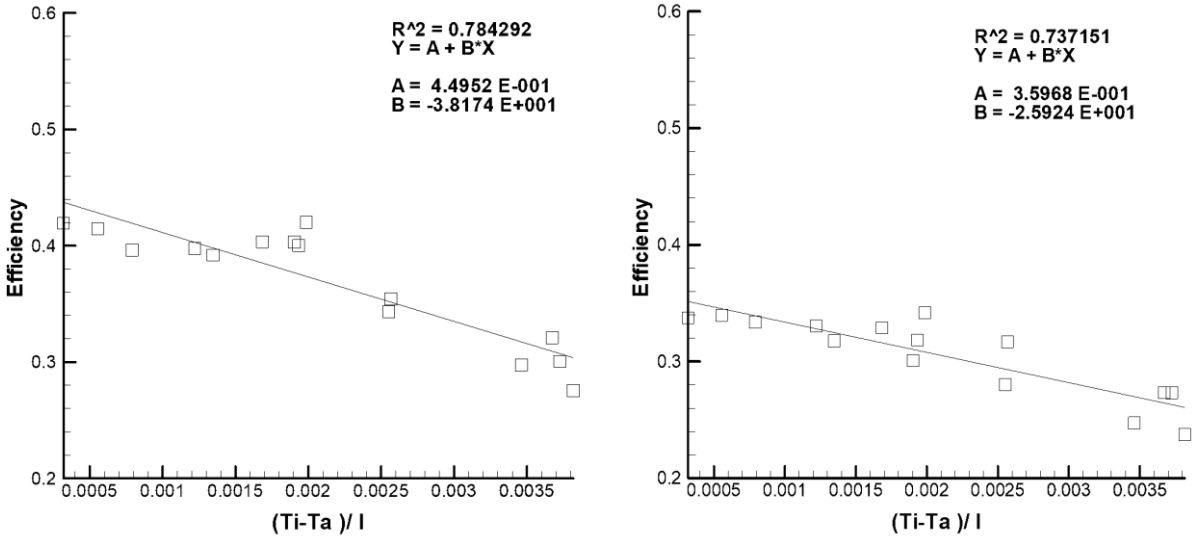

Fig. 5: Variation of instantaneous efficiencies for perforated and corrugate plates with a temperature parameter (Ti–Ta)/I, for m= 0.016 kg/s.

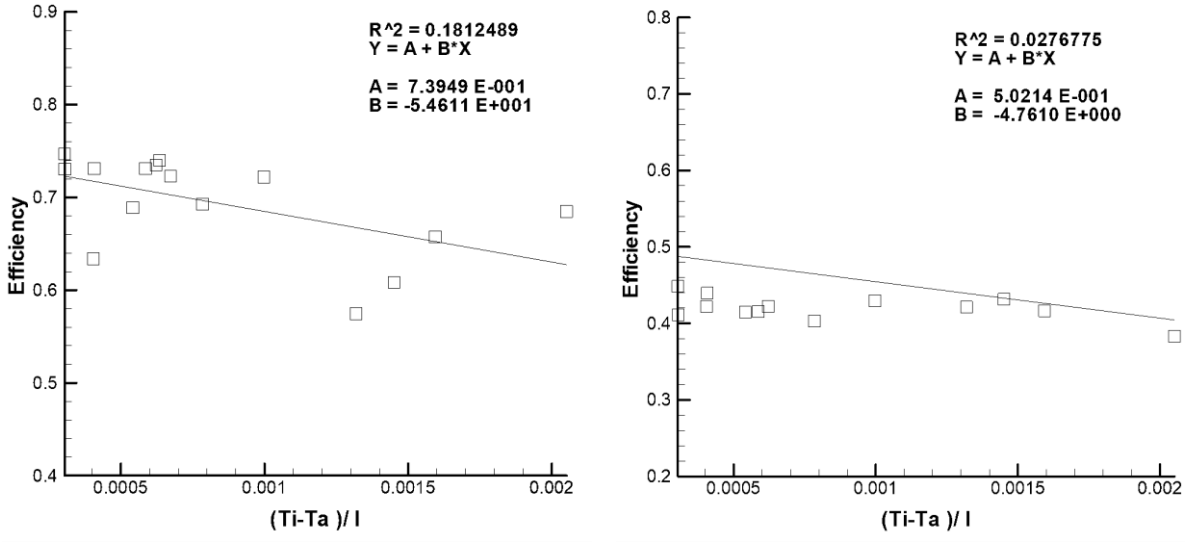

Fig. 6: Variation of instantaneous efficiencies for perforated and corrugate plates with a temperature parameter (Ti–Ta)/I, for m= 0.032 kg/s.

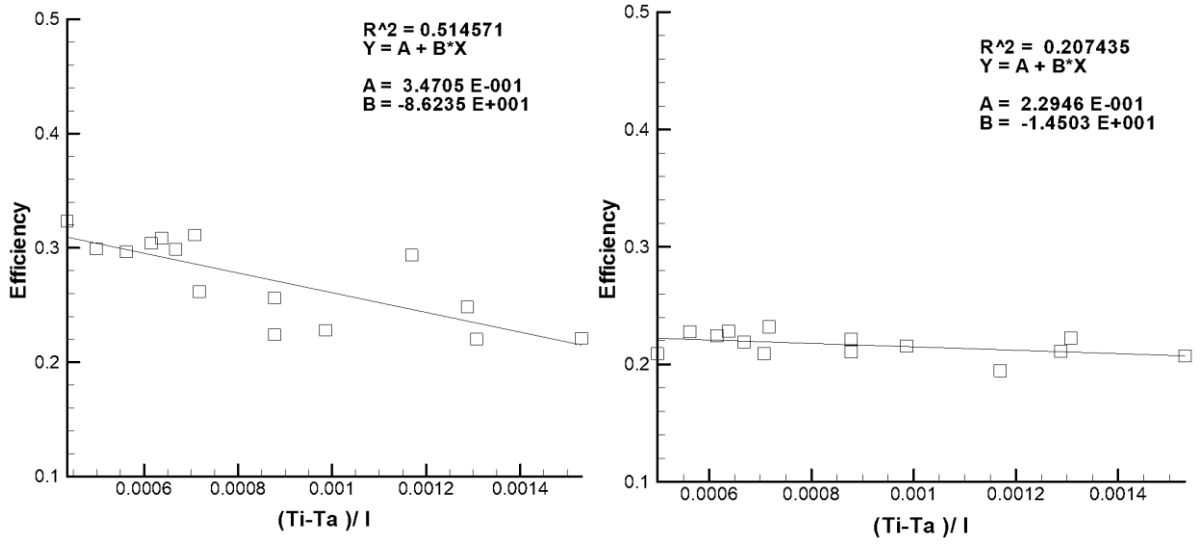

Fig. 7: Variation of instantaneous efficiencies for wavy and punched plates with a temperature parameter (Ti–Ta)/I, for m= 0.016 kg/s.

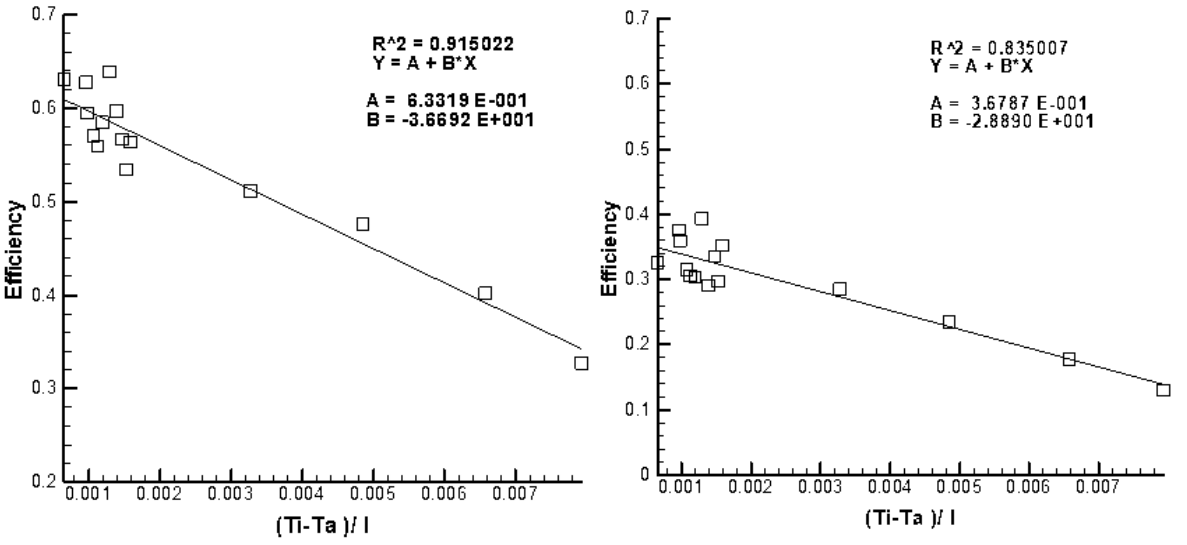

Fig. 8: Variation of instantaneous efficiencies for wavy and punched plates with a temperature parameter $(T_i–T_a)/I$, for m= 0.023 kg/s.

Table 3: The empirical relations and regression coefficients for the variation of the $(T_i–T_a)/I$ with the thermal efficiencies, under working conditions.

Instantaneous efficiency	Conditions	Functions	Coefficients
ṁ= 0.016 kg/s	Perforated plate	ηi = 0.449+(-38.18)×$(T_i - T_a/I)$	R^2 = 0.7842
	Corrugate plate	ηi = 0.359 +(-25.924)×$(T_i - T_a/I)$	R^2 = 0.7371
ṁ = 0.032 kg/s	Perforated plate	ηi = 0 739+(-54.611)×$(T_i - T_a/I)$	R^2 = 0.1812
	Corrugate plate	ηi = 0.502+(-4.610)×$(T_i - T_a/I)$	R^2 = 0.0276
ṁ = 0.016 kg/s	Perforated plate	ηi = 0. 347 +(-86.235)×$(T_i - T_a/I)$	R^2 = 0.5145
	Corrugate plate	ηi = 0. 229 +(-14.503)×$(T_i - T_a/I)$	R^2 = 0.2074
ṁ = 0.032 kg/s	Perforated plate	ηi = 0.633+(-36.692)×$(T_i - T_a/I)$	R^2 = 0.9150
	Corrugate plate	ηi = 0.367+(-28.890)×$(T_i - T_a/I)$	R^2 = 0.1592

The variable λ is defined as the following:

$$\lambda = \frac{A_p}{\nu\, A_e\, \rho\, C_p} = \frac{A_p}{\dot{m}\, C_p} \quad (11)$$

Substituting the values of B, A, and λ (Eq. 11) into Eq. 10, the ambient temperature was equal to the inlet temperature ($T_i = T_a$), then Eq. 10 was given as Eq. 12:

$$T_o = T_a + A\lambda I \quad (12)$$

The empirical equations for outlet temperatures of different absorber plates are based on the parameters A and λ, as they relate to solar intensity and inlet temperature under specific operating conditions.

Perforated plate (m= 0.016 kg/s): $T_o = T_a + 0.347 \times I$ (13)

Corrugate plate (m= 0.016 kg/s): $T_o = T_a + 0.021 \times I$ (14)

Perforated plate (m= 0.032 kg/s): $T_o = T_a + 0.026 \times I$ (15)

Corrugate plate (m= 0.032 kg/s): $T_o = T_a + 0.019 \times I$ (16)

Wavy plate (m= 0.016 kg/s): $T_o = T_a + 0.023 \times I$ (17)

Punched plate (m= 0.016 kg/s): $T_o = T_a + 0.014 \times I$ (18)

Wavy plate (m= 0.032 kg/s): $T_o = T_a + 0.024 \times I$ (19)

Punched plate (m= 0.032 kg/s): $T_o = T_a + 0.014 \times I$ (20)

4.6 Experimented measured outlet temperature and predicted outlet air temperature

Figs. 9 and 10 present the experimental measurements of outlet air temperature (T_o) alongside the predicted outlet air temperature (T_o, Simulated), calculated using Eqs. 13-20. Validation was performed for all cases. Solar collectors show a maximum discrepancy of 7 °C between the predicted and experimental values throughout the working day. The results demonstrate a satisfactory agreement between the simulated and experimental data. In general, the rise in outlet temperature is influenced by solar radiation intensity and the degree of heat loss to the surrounding atmosphere, as previously noted by researchers Vaziri *et al.*[20] and Mahmood.[13]

5. Numerical simulation methodology

5.1 Geometry description

The SAH used in the current simulation was designed and modeled using SOLIDWORKS 2018 software, as shown in Fig. 11. For the fabrication and testing process, two distinct absorber plate configurations were utilized: a wavy flat plate and a corrugated flat plate.

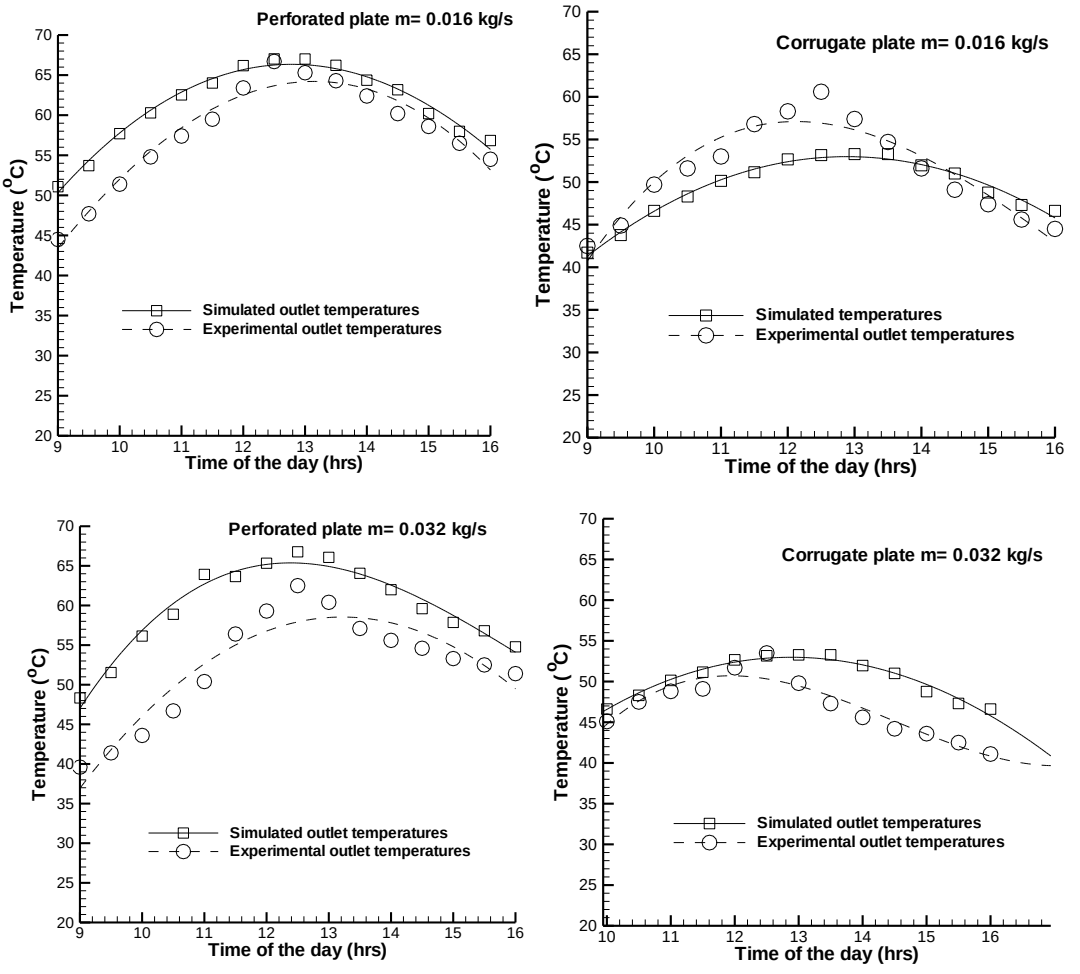

Fig. 9: Experimented measured outlet temperature and predicted outlet air temperature for perforated plate and corrugate plate.

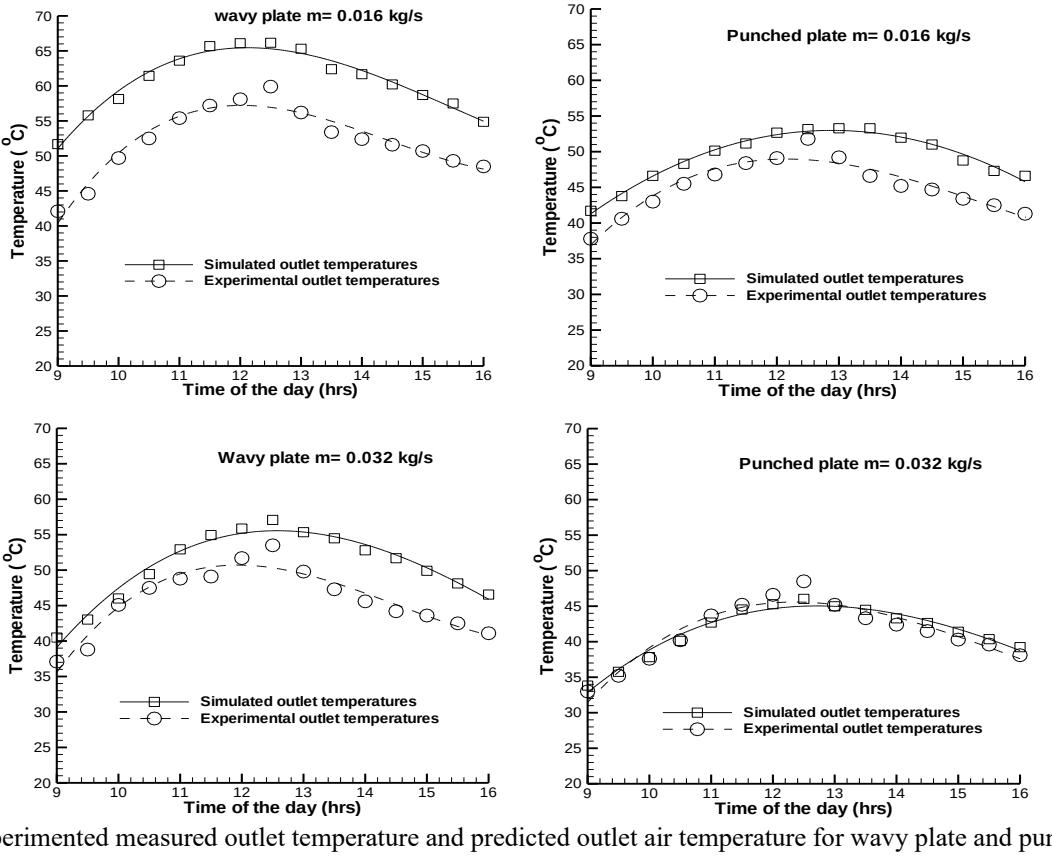

Fig. 10: Experimented measured outlet temperature and predicted outlet air temperature for wavy plate and punched plate.

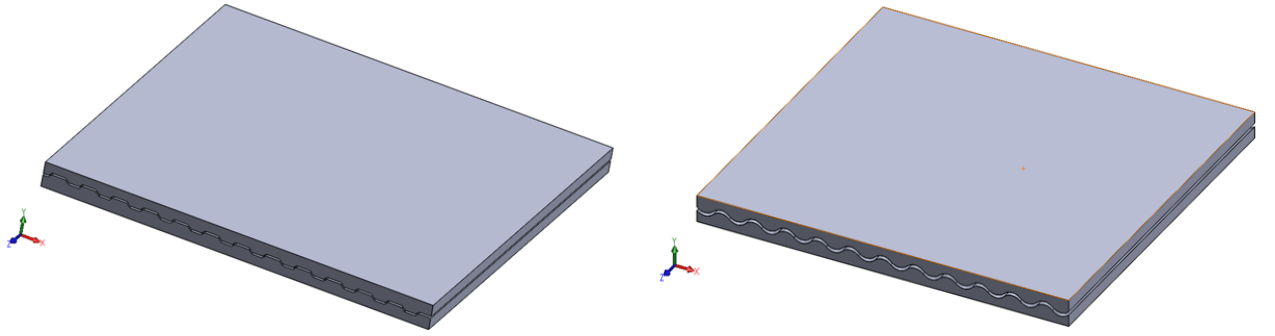

Fig. 11: Schematic of dual-flow flat absorber plate (wavy and corrugated).

5.2 Boundary conditions

The boundary conditions for the numerical simulation of the SAH were implemented using ANSYS Fluent 2020 R2 software (as shown in Fig. 12). The following conditions were applied:

1. Airflow Rate: The mass airflow rate was varied between 0.016 and 0.032 kg/s, with the inlet air temperature maintained at a constant value of 34 °C.
2. Outlet Pressure: The outlet of the air duct was set to a default atmospheric pressure of 0 Pa.
3. Solar Intensity: A uniform heat flux 1007 W/m^2, representing solar intensity, was applied to the top surface of the duct.
4. Insulation: All other walls of the air heater were treated as insulated boundaries to minimize heat losses.
5. Temperature Distribution: The numerical simulation calculated the temperature of the airflow and the absorber plate at the outlet based on these boundary conditions.

This setup ensured realistic simulation of the dual-flow SAH's thermal performance under standard operating conditions.

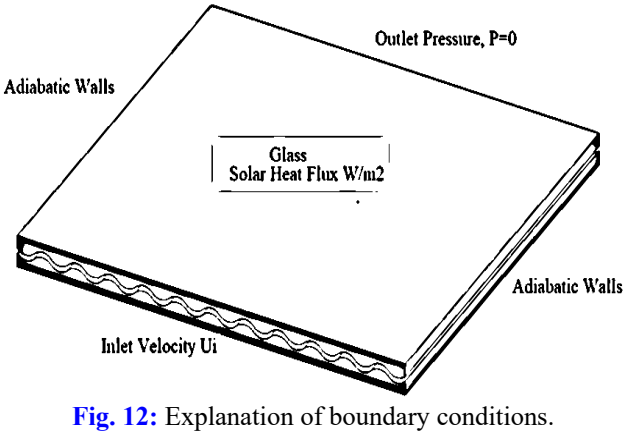

Fig. 12: Explanation of boundary conditions.

5.3 Governing equations

The Navier-Stokes equations, which represent the conservation of mass, momentum, and energy, are fundamental in describing fluid motion and heat transfer. These equations (Eqs. 21-25) specifically address turbulent and incompressible flows.[24,25]

Conservation of mass:

$$\frac{\partial}{\partial t}(\rho) + \frac{\partial}{\partial x}(\rho u) + \frac{\partial}{\partial y}(\rho v) = 0 \tag{21}$$

Conservation of momentum:

(1) x-momentum

$$\rho\left(\frac{\partial u}{\partial t} + u\frac{\partial u}{\partial x} + v\frac{\partial u}{\partial y} + w\frac{\partial u}{\partial y}\right) = -\frac{\partial p}{\partial x} + \mu_{eff}\left(\frac{\partial^2 u}{\partial x^2} + \frac{\partial^2 u}{\partial y^2} + \frac{\partial^2 u}{\partial z^2}\right) + S_u \tag{22}$$

(2) y-momentum

$$\rho\left(\frac{\partial v}{\partial t} + u\frac{\partial v}{\partial x} + v\frac{\partial v}{\partial y} + w\frac{\partial v}{\partial y}\right) = -\frac{\partial p}{\partial y} + \mu_{eff}\left(\frac{\partial^2 v}{\partial x^2} + \frac{\partial^2 v}{\partial y^2} + \frac{\partial^2 v}{\partial z^2}\right) + S_v \tag{23}$$

(3) z-momentum

$$\rho\left(\frac{\partial w}{\partial t} + u\frac{\partial w}{\partial x} + v\frac{\partial w}{\partial y} + w\frac{\partial w}{\partial y}\right) = -\frac{\partial p}{\partial z} + \mu_{eff}\left(\frac{\partial^2 w}{\partial x^2} + \frac{\partial^2 w}{\partial y^2} + \frac{\partial^2 w}{\partial z^2}\right) + S_u \tag{24}$$

Energy equation:

$$\frac{\partial T}{\partial t} + \frac{\partial uT}{\partial x} + \frac{\partial vT}{\partial y} + \frac{\partial wT}{\partial z} = \frac{1}{\rho}\frac{\partial}{\partial x}\left[\Gamma_{eff}\frac{\partial T}{\partial x}\right] + \frac{1}{\rho}\frac{\partial}{\partial y}\left[\Gamma_{eff}\frac{\partial T}{\partial y}\right] + \frac{1}{\rho}\frac{\partial}{\partial z}\left[\Gamma_{eff}\frac{\partial T}{\partial z}\right] \tag{25}$$

To accurately predict air movement and contaminant dispersion within an SAH, selecting an appropriate turbulence model from the available options is crucial. The two-equation renormalization group (RNG) standard k-ε turbulence model was employed to simulate the turbulent airflow in the SAH. The standard k-ε model is described through the following equations (Eqs. 26-32) for turbulent kinetic energy (k):[24,25]

$$\frac{\partial k}{\partial t} + \frac{\partial uk}{\partial x} + \frac{\partial vk}{\partial y} + \frac{\partial wk}{\partial z} = \frac{1}{\rho}\frac{\partial}{\partial x}\left[\left(\mu_{eff} + \frac{\mu_t}{\sigma_k}\right)\frac{\partial k}{\partial x}\right] + \frac{1}{\rho}\frac{\partial}{\partial y}\left[\left(\mu_{eff} + \frac{\mu_t}{\sigma_k}\right)\frac{\partial k}{\partial y}\right] + + \frac{1}{\rho}\frac{\partial}{\partial z}\left[\left(\mu_{eff}\mu + \frac{\mu_t}{\sigma_k}\right)\frac{\partial k}{\partial z}\right]\frac{1}{\rho}(G_k + G_b) - \varepsilon \tag{26}$$

Dissipation rate (ε):

$$\frac{\partial \varepsilon}{\partial t} + \frac{\partial u\varepsilon}{\partial x} + \frac{\partial v\varepsilon}{\partial y} + \frac{\partial w\varepsilon}{\partial z} = \frac{1}{\rho}\frac{\partial}{\partial x}\left[\left(\mu_{eff} + \frac{\mu_t}{\sigma_\varepsilon}\right)\frac{\partial \varepsilon}{\partial x}\right] + \frac{1}{\rho}\frac{\partial}{\partial y}\left[\left(\mu_{eff} + \frac{\mu_t}{\sigma_\varepsilon}\right)\frac{\partial \varepsilon}{\partial y}\right] + \frac{1}{\rho}\frac{\partial}{\partial z}\left[\left(\mu_{eff} + \frac{\mu_t}{\sigma_\varepsilon}\right)\frac{\partial \varepsilon}{\partial z}\right] + C_1\frac{\varepsilon}{\rho k}(G_k + C_3 G_b) - C_2\frac{\varepsilon^2}{k} \tag{27}$$

μ_{eff} is the effective viscosity coefficient:

$$\mu_{eff} = \mu + \mu_t \tag{28}$$

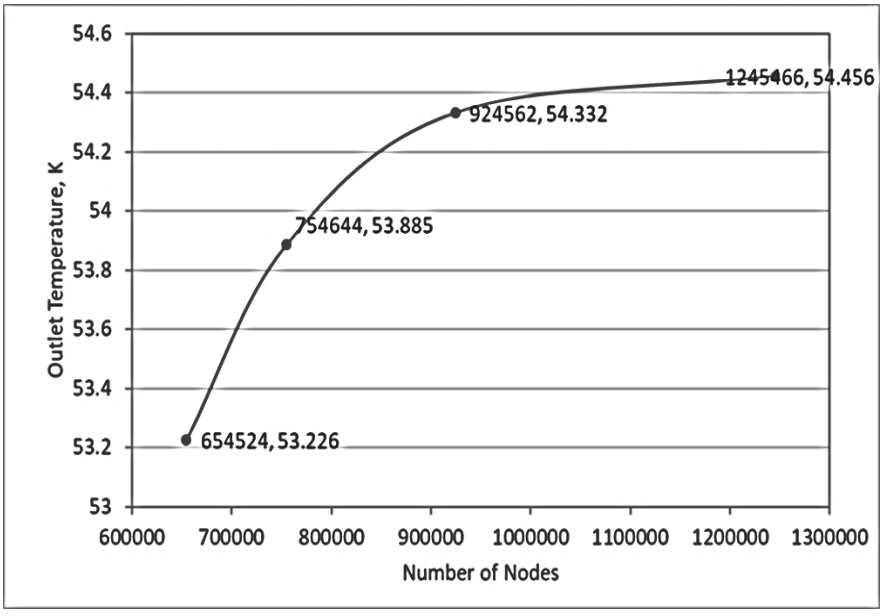

Fig. 13: Grid independence study of the 3D simulations.

Γ_{eff} is the effective diffusion coefficient:

$$\Gamma_{eff} = \frac{\mu}{p_r} + \frac{\mu_t}{\sigma_t} \quad (29)$$

μ_t is the eurbulent viscosity:

$$\mu_t = \rho C_\mu \frac{k^2}{\varepsilon} \quad (30)$$

G_k is the Kinetic energy generation by shear:

$$G_k = \mu_t \left(2\left[\left(\frac{\partial u}{\partial x}\right)^2 + \left(\frac{\partial v}{\partial y}\right)^2\right] + \left(\frac{\partial u}{\partial y} + \frac{\partial v}{\partial x}\right)^2\right) \quad (31)$$

G_b is the Kinetic energy generated by buoyancy:

$$G_b = \frac{\mu_t}{\sigma_t}\frac{\partial T}{\partial y} g\beta \quad (32)$$

where C_μ represents a big Reynolds number flow value for an empirical constant. The working fluid, air, generates a uniform heat flux on the absorber wall and is characterized by a Prandtl number of 0.7. To ensure the accuracy of the selected k-ε turbulence model, a comparison was made with the k-ω model and experimental results, as depicted in Fig. 13 and summarized in Table 4. The results indicate that the k-ε model closely aligns with the experimental data. Additionally, Table 4 provides the values of the constants used in the k-ε model, reinforcing its reliability in the current study.[26,27]

Table 4: Values of constants in the k-ε models.[25]

Values of constants in the model					
C_μ	C_1	C_2	C_3	σ_ε	σ_k
0.09	1.44	192	1.0	1.3	1.0

5.4 Mesh generation and independence study

To create the computational domain, the mesh was generated using ANSYS Fluent Workbench 2020 R2 to develop mesh files. The airspace, representing the upstream and downstream flow within the SAH, was modeled with a tetrahedral mesh structure. Fig. 14 illustrates the mesh architecture, which consists of 924,562 nodes distributed along the *x*, *y*, and *z* axes for a single segment of the SAH.

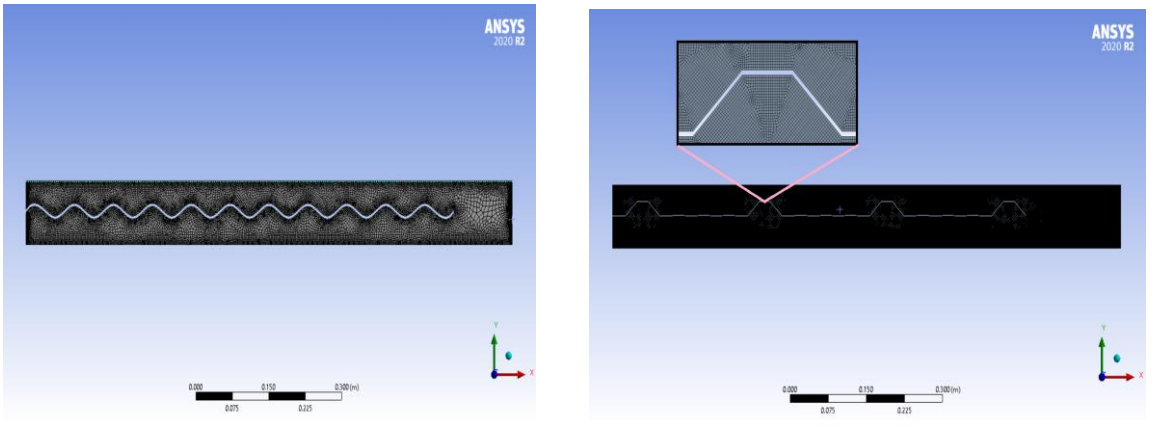

Wavy plate parallel path direction Trapezoidal corrugated plate

Fig. 14: Computational domain mesh of the dual-flow collector cavity model.

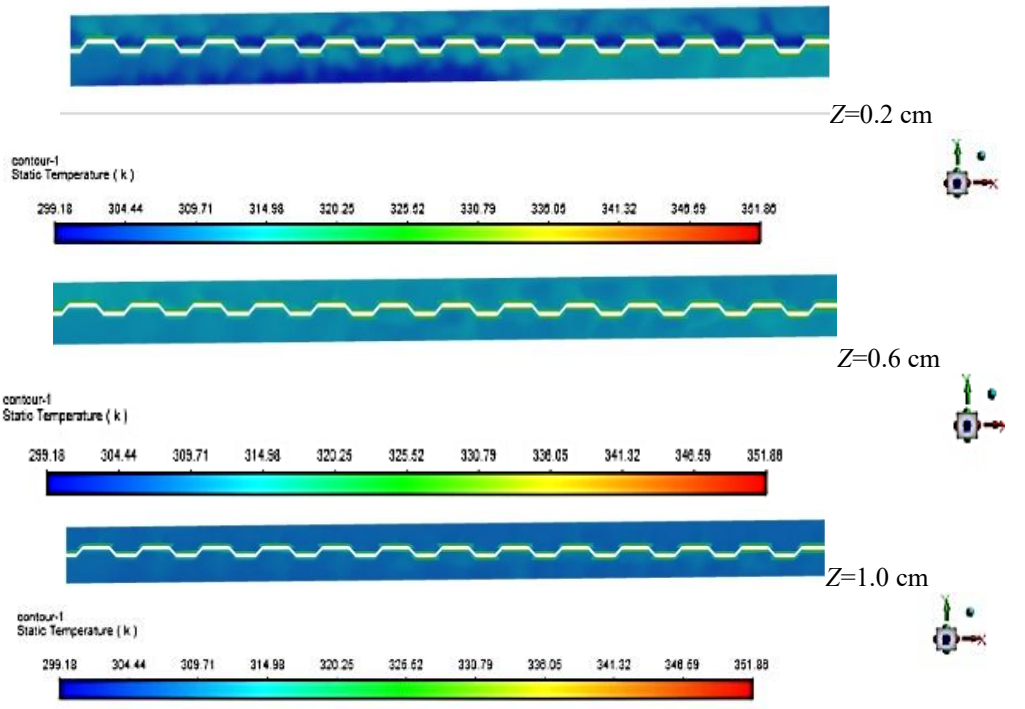

Fig. 15: Temperature distribution of air in corrugated absorber plate, at m=0.016 kg/s, I=1007 in *z*-axis.

For the grid independence study in the 3D simulations, four mesh resolutions (coarse, medium, fine, and finer) were evaluated, with their specifications detailed in Table 5. Each component of the loop employed a block strategy for mesh generation. To ensure accuracy near the walls, the mesh aimed for a near-wall cell size with a y+ value of less than 1. Cells were clustered closer to the wall with an expansion ratio of 1.06 toward the center. A mesh sensitivity analysis was conducted by comparing the outlet temperature profiles derived from simulations with varying node counts. Among the four mesh configurations tested, the grid with 1,245,466 finite volumes was selected for further simulations. This choice balanced computational cost and accuracy, making it an efficient and reliable option for subsequent analyses.

Table 5: Characteristics of all the 2D meshes considered for the SAH cavity

No.	Mesh type	Nodes	To (ºC)
1.	Coarse	654524	53.226
2.	Medium	754644	53.885
3.	Fine	924562	54.332
4.	Finer	1245466	54.456

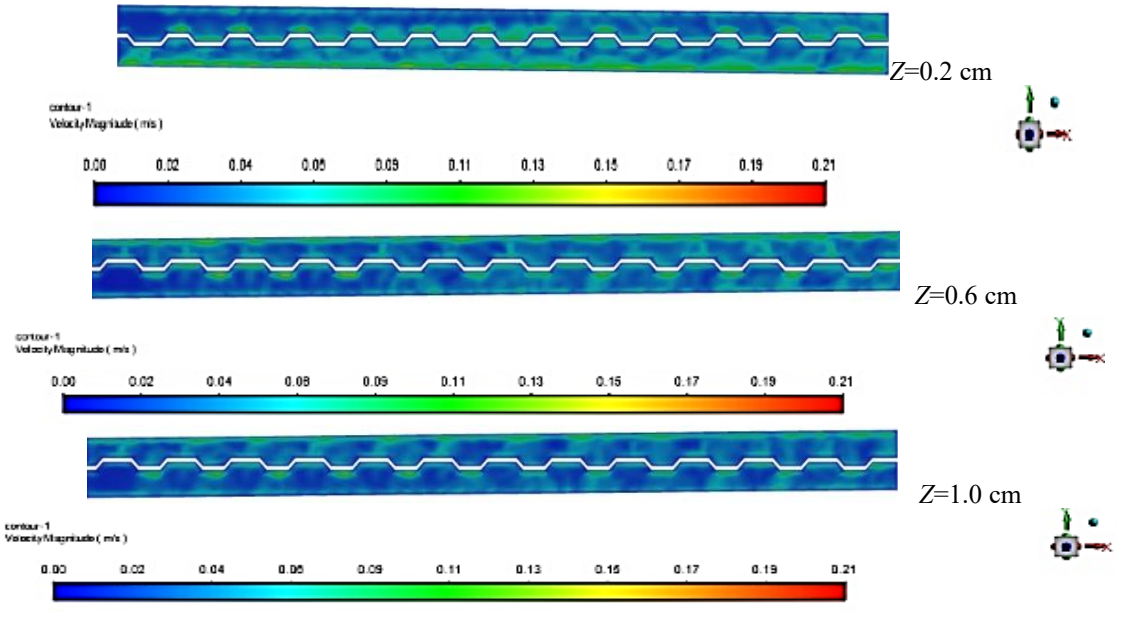

Fig. 16: Velocity distribution of air in corrugated absorber plate, at m=0.016 kg/s, I=1007 *z*-axis.

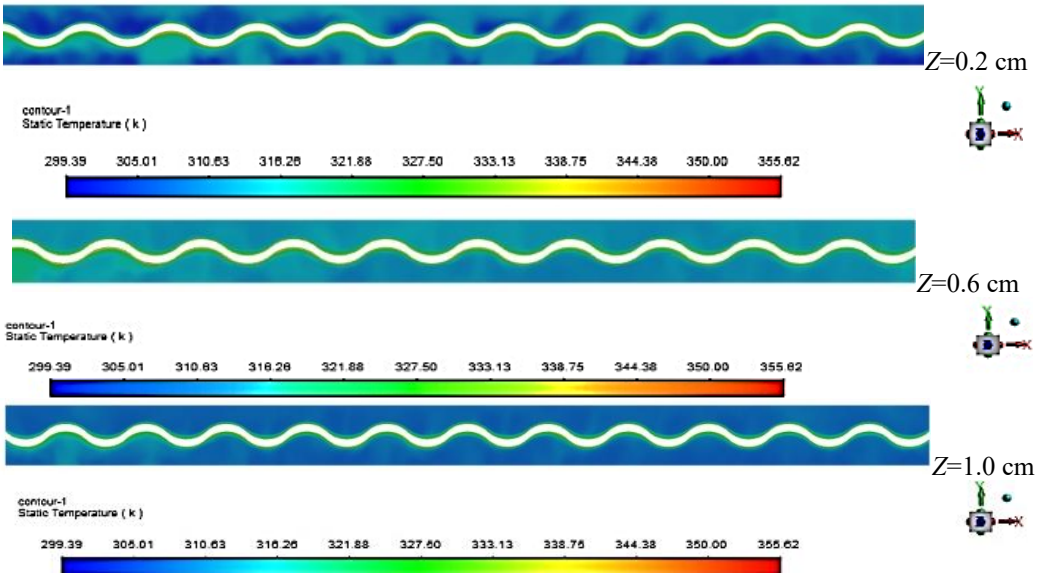

Fig. 17: Temperature distribution of air in wavy absorber plate, at m=0.016 kg/s, I=1007 *z*-axis.

5.5 Temperature and velocity distribution of air on the corrugated plate

Fig. 15 shows the temperature distribution inside the solar channel with a corrugated absorber plate in the Z direction for 0.016 kg/s and a maximum solar intensity of 1007 W/m^2. For the corrugated plate, the maximum temperature was from 63 ^{o}C from z = 0.2 to 1 cm. Fig. 16 shows the velocity distribution inside the solar channel on the corrugated absorber plate in the Z direction for 0.016 kg/s and a maximum solar intensity of 1007 W/m^2. For the corrugated plate, the maximum velocity was 0.12 m/s (z = 0.2 to 1 cm).

5.6 Temperature and velocity distribution of air on a wavy plate

Fig. 17 illustrates the temperature distribution within the solar channel featuring a corrugated absorber plate along the Z-direction, at a mass flow rate of 0.016 kg/s and a maximum solar intensity of 1007 W/m². For the wavy plate, the highest temperature recorded was 61 ^{o}C, observed in the range of z=0.2 to 1 cm. Fig. 18 presents the velocity distribution within the solar channel on a corrugated absorber plate along the Z-direction, under the same conditions. The velocity reached 0.09 m/s within the range of z=0.2 to 1 cm.

A comparison of the numerical and experimental results shows that the numerical model predicts slightly higher outlet temperatures for the corrugated and wavy designs. This difference can be attributed to the numerical model assuming an equal distribution of absorbed heat between the upper and lower passing airflows. In contrast, in the experimental case, the heat gain of the lower passing airflow is reduced due to the heat transfer occurring in the upper absorber plates.

The highest performance achieved in terms of temperature differences and thermal efficiency in the current study is compared with a similar investigation involving a double-pass flow system with a perforated absorber plate, as presented in Table 6.

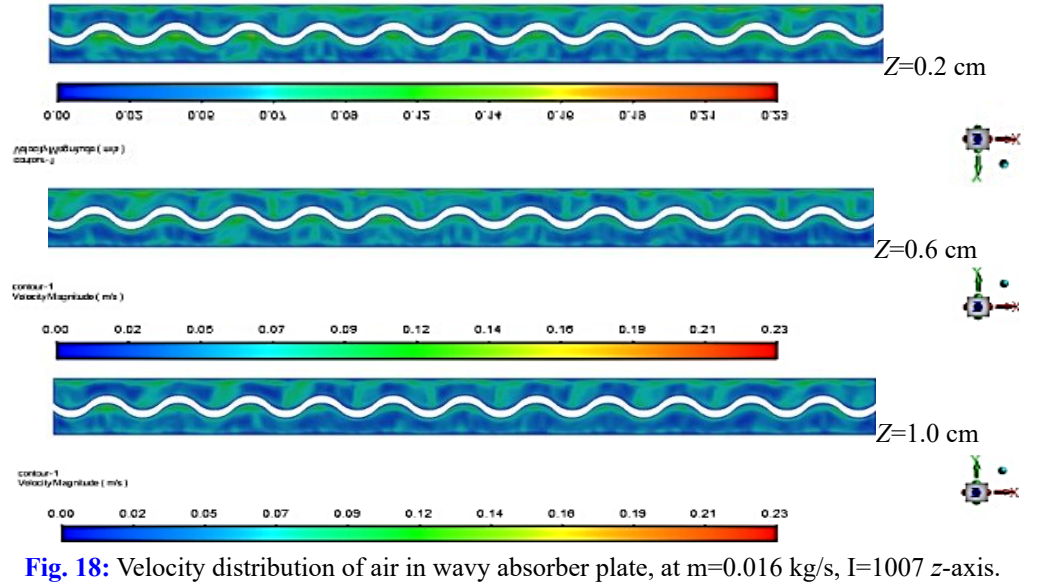

Fig. 18: Velocity distribution of air in wavy absorber plate, at m=0.016 kg/s, I=1007 *z*-axis.

Table 6: Comparison of temperature differences and thermal efficiency of the current study with previous literature.

Researcher	Collector type	Dimensions (m^3)	Solar intensity W/m^2	**Δ**T °C	Air flow rate kg/s	η%
Vaziri *et al.* [20]	Experimental performance of perforated glazed SAHs	0.9×0.9×0.3	906	16.2	0.036	82
Nowzari *et al.*[22]	Experimental Quarter perforated with plexiglas cover	1×1.5×0.05	724	24.6	0.037	56
Mahmood[13]	Experimental Perforated plate glazed heater (bed angle 47°)	1.5×1×0.05	920	23	0.045	66
Arunkumar *et al.*[11]	Experimental Perforation Hole on the Absorber in a SAH	1.0×0.20×0.03	950	43	0.038	87.3
Present work	Experimental measured of perforated plate	1.14×1.09×0.045	1007	29	0.032	75

6. Conclusion

The novelty of this study lies in its unique approach to combining corrugated and perforated plate designs for thermal analysis, which has not been explored in prior research. By evaluating these configurations under identical outdoor conditions, this research provides a comprehensive comparison of four innovative assemblies, identifying the most effective design for optimizing the thermal performance of solar systems.

1. An outdoor experimental study was conducted to evaluate the outlet temperature and thermal efficiency of a double-pass SAH utilizing a perforated plate, corrugated plate, wavy plate, and punched plate as the absorber plate. The prototype was designed and fabricated in Baghdad, Iraq, to enhance the performance of conventional thermal efficiency collectors. The system featured and testing were carried out over four clear days, with maximum solar intensity on the collector cover reaching 1007 W/m² and ambient air temperatures ranging from 24 to 32 °C.

2. Ambient air temperature, inlet temperature and solar intensity seem same data for experimental work for corrugate and perforated plates, the outlet temperature and thermal efficiencies demonstrated for perforated plate slight increase than corrugate plate, that can be attributed to the following: the perforations created localized turbulence, disrupting the boundary layer and enhancing heat transfer by allowing more effective energy exchange between the plate surface and the passing air. The perforated plate's ability to induce turbulence near the plate surface may reduce the temperature gradient between the plate and the surrounding air, minimizing thermal losses.

3. The increase in outlet temperature and thermal efficiency for a wavy plate compared to a punched (semi perforated) plate can be attributed that the undulating structure increases the surface area available for heat transfer, allowing more energy to be absorbed and transferred to the passing air, while punched plate less effective surface area available for direct heat conduction and convection.

4. The experimental results were compared with the predictions from the theoretical model, showing good agreement with the monitored data. The maximum discrepancy between the experimental and predicted values was found to be 7 °C across all days of observation.

5. A comparison between the numerical and experimental results reveals that the numerical model predicts slightly higher outlet temperatures for the corrugated and wavy designs. This discrepancy arises because the numerical model assumes an even distribution of absorbed heat between the upper and lower airflow channels. However, in the experimental setup, the heat gain of the lower airflow is diminished due to heat transfer occurring primarily through the upper absorber plates. A comparison of experimental results with theoretical model predictions showed good agreement, with a maximum deviation of 5 °C observed across all tested days.

6. The thermal performance of the system was notably improved by incorporating a double-pass collector, which increased the air path length, allowing for greater heat absorption while reducing heat losses to the environment.

Conflict of Interest

There is no conflict of interest.

Supporting Information

Not applicable.

Nomenclature

Ae	Exit area (m^2)
A_P	Surface area of absorber plate (m^2).
C	Conversion factor
C_1	Empirical constant
C_2	Empirical constant
C_3	Empirical constant
C_μ	Reynolds number empirical constant
C_p	Specific heat of air (J/kg °C)
D	Hydraulic diameter of duct (m)
f	Friction factor (-)
Fo	Heat removal factor (-)
Fp	Collector efficiency factor (-)
F_R	Heat removal coefficient
G_b	Kinetic energy generation by buoyancy
G_k	Kinetic energy generation by shear
I	Solar intensity (W/m^2)
k	Turbulent kinetic energy (m^2/s^2)
K	Thermal conductivity of air (W/m. °C)
L	length of test section (m)
$\dot{m}$	Mass flow rate of air (kg/s)
P	Pressure (Pa)
Q	Specific heat capacity (W)
Qu	Useful heat gain (W)
S	Body force per unit volume (N/m^3)
t	Time (sec)
Ti	Temperature of fluid at inlet (°C)
To	Temperature of fluid at outlet (°C)
Tp	Temperature of absorber plate (°C)
Ta	Ambient temperature of flowing fluid (°C)
ΔT	Air temperature rises across the duct (°C)
ΔT/I	Temperature rise parameter (m^2 K/W)
u,v,w	Velocity at x,y,z direction (m/s)
U_L	Overall heat loss coefficient (W/m^2 °C)
ρ	Fluid density (kg/m^3)
ε	Rate of dissipation of turbulent kinetic energy (W/m^3)
μ	Dynamic viscosity (kg/m·s)
Φ	Dissipation function (W/m^3)
σε, σk	Empirical constant
ηi	Instantaneous thermal efficiency
η_{th}	Thermal efficiency
τα	Effective transmittance absorbance
μ_t	Turbulent viscosity (kg/m·s)
Γ_{eff}	Effective diffusion coefficient (m^2/s)
μ_{eff}	Effective viscosity coefficient (kg/m·s)

References

[1] F. A. Kareem, N. S. Lafta, A. J. Mahmood, Numerical investigation flat plate solar collector performance in Baghdad base on exergy analysis, *International Journal of Exergy*, 2023, **42**, 20-37, doi: 10.1504/ijex.2023.134286.

[2] K. M. Pandey, R. Chaurasiya, A review on analysis and development of solar flat plate collector, *Renewable and Sustainable Energy Reviews*, 2017, **67**, 641-650, doi: 10.1016/j.rser.2016.09.078.

[3] V. Dabra, A. Yadav, Performance analysis and comparison of glazed and unglazed solar air collector, *Environment, Development and Sustainability*, 2020, **22**, 863-881, doi: 10.1007/s10668-018-0223-y.

[4] A. S. Sreeharsha, V. P. Chandramohan, S. Abraham, Influence of pentagonal corrugated absorber sheet on heat transfer behavior of solar air collector: numerical analysis with optimized corrugation dimensions, *Journal of Thermal Analysis and Calorimetry*, 2024, **149**, 15025-15039, doi: 10.1007/s10973-024-13837-7.

[5] A. F. Abed, R. B. Dahham, N. A. W. Hashim, R. F. Hamad, Performance enhancement of a solar air collector using a V-corrugated absorber, *Journal of Aerospace Technology and Management*, 2023, **15**, e1423, doi: 10.1590/jatm.v15.1304.

[6] M. Hedayatizadeh, F. Sarhaddi, A. Safavinejad, F. Ranjbar, H. Chaji, Exergy loss-based efficiency optimization of a double-pass/glazed v-corrugated plate solar air heater, *Energy*, 2016, **94**, 799-810, doi: 10.1016/j.energy.2015.11.046.

[7] L. T. Zubairi, M. Danismaz, N. J. Yasin, W. A. M. Al-Shohani, Comparative analysis of thermal performance in dual-flow solar air heaters utilizing diverse absorber plates, *International Journal of Heat and Technology*, 2023, **41**, 1014-1034, doi: 10.18280/ijht.411423.

[8] H. Hassan, S. Abo-Elfadl, Experimental study on the performance of double pass and two inlet ports solar air heater (SAH) at different configurations of the absorber plate, *Renewable Energy*, 2018, **116**, 728-740, doi: 10.1016/j.renene.2017.09.047.

[9] A. A. Gitan, A. Mohammed, Assessment of perforated double-pass solar air heater using parametric interaction analysis for performance enhancement in solar thermal systems, *Tikrit Journal of Engineering Sciences*, 2024, **31**, 177-191, doi: 10.25130/tjes.31.3.17.

[10] R. Vijayakumar, R. V. Kumar, P. Madhu, Investigation on energy, economic, and environmental aspects of double-pass solar air heater, *Environmental Science and Pollution Research*, 2024, **31**, 39406-39420, doi: 10.1007/s11356-024-33786-w.

[11] S. Arunkumar H., S. Kumar, K. V. Karanth, A numerical study on the performance of different shaped perforation hole on the absorber duct insert in a solar air heater, *Engineered Science*, 2022, **18**, 234-242, doi: 10.30919/es8d644.

[12] H. Farzan, E. H. Zaim, Thermal analysis of a new double-pass solar air heater using perforated absorber and porous materials: An experimental study, *Thermal Science and Engineering Progress*, 2023, **38**, 101680, doi: 10.1016/j.tsep.2023.101680.

[13] A. J. Mahmood, An experimental study on energy and

exergy for glazed and unglazed solar system with perforated absorber plate and wire mesh layers, *International Journal of Renewable Energy Research*, 2019, **9**, 1900-1911, doi: 10.20508/ijrer.v9i4.9994.g7808.
[14] A. J. Mahmood, Thermal evaluation of a double-pass unglazed solar air heater with perforated plate and wire mesh layers, *Sustainability*, 2020, **12**, 3619, doi: 10.3390/su12093619.
[15] O. R. Alomar, H. M. Abd, M. M. Mohamed Salih, Efficiency enhancement of solar air heater collector by modifying jet impingement with v-corrugated absorber plate, *Journal of Energy Storage*, 2022, **55**, 105535, doi: 10.1016/j.est.2022.105535.
[16] R. B. Pérez, A. M. Pérez, D. S. Suárez, Influence of the punched holes on thermohydraulic performance and flow pattern of rectangular channels with a pair of perforated vortex generators, *International Journal of Heat and Mass Transfer*, 2022, **184**, 122291, doi: 10.1016/j.ijheatmasstransfer.2021.122291.
[17] A. Priyam, P. Chand, Thermal and thermohydraulic performance of wavy finned absorber solar air heater, *Solar Energy*, 2016, **130**, 250-259, doi: 10.1016/j.solener.2016.02.030.
[18] S. Singh, S. K. Chaurasiya, B. S. Negi, Efficient design of a wavy channel embedded with porous media for solar air heating, *Energy Sources, Part A: Recovery, Utilization, and Environmental Effects*, 2021, **43**, 2738-2754, doi: 10.1080/15567036.2020.1850930.
[19] A. Priyam, D. P. Chand, D. Shaw, N. Jamshedpur, Thermal performance comparison of solar air heater having wavy fin and longitudinal fin, *International Journal of Engineering Research and Technology*, 2015, **V4**, 152-157, doi: 10.17577/ijertv4is090190.
[20] R. Vaziri, M. Ilkan, F. Egelioglu, Experimental performance of perforated glazed solar air heaters and unglazed transpired solar air heater, *Solar Energy*, 2015, **119**, 251-260, doi: 10.1016/j.solener.2015.06.043.
[21] P. Dhiman, N. S. Thakur, S. R. Chauhan, Thermal and thermohydraulic performance of counter and parallel flow packed bed solar air heaters, *Renewable Energy*, 2012, **46**, 259-268, doi: 10.1016/j.renene.2012.03.032.
[22] R. Nowzari, L. B. Y. Aldabbagh, F. Egelioglu, Single and double pass solar air heaters with partially perforated cover and packed mesh, *Energy*, 2014, **73**, 694-702, doi: 10.1016/j.energy.2014.06.069.
[23] A. J. Mahmood, Experimental study for improving unglazed solar system, *Cogent Engineering*, 2021, **8**, 1961564, doi: 10.1080/23311916.2021.1961564.
[24] R. Shaheed, A. Mohammadian, H. Kheirkhah Gildeh, A comparison of standard k-ε and realizable k-ε turbulence models in curved and confluent channels, *Environmental Fluid Mechanics*, 2019, **19**, 543-568, doi: 10.1007/s10652-018-9637-1.
[25] B. E. Launder, D. B. Spalding, The numerical computation of turbulent flows, *Computer Methods in Applied Mechanics and Engineering*, 1974, **3**, 269-289, doi: 10.1016/0045-7825(74)90029-2.
[26] H. Wang, Z. Zhai, Analyzing grid independency and numerical viscosity of computational fluid dynamics for indoor environment applications, *Building and Environment*, 2012, **52**, 107-118, doi: 10.1016/j.buildenv.2011.12.019.
[27] X. Wang, L. Zhang, Y. Chang, Y. Song, L. Wang, Numerical simulation study on heat performance and pressure loss of solar air heater with sinusoidal baffles, *AIMS Energy*, 2024, **12**, 617-638, doi: 10.3934/energy.2024029.